

## Ionospheric vertical correlation distances

Forsythe, Victoriya V.; Azeem, Irfan; Crowley, Geoff; Themens, David R.

DOI:

[10.1029/2020RS007177](https://doi.org/10.1029/2020RS007177)

License:

None: All rights reserved

*Document Version*

Publisher's PDF, also known as Version of record

*Citation for published version (Harvard):*

Forsythe, VV, Azeem, I, Crowley, G & Themens, DR 2021, 'Ionospheric vertical correlation distances: estimation from ISR data, analysis, and implications for ionospheric data assimilation', *Radio Science*, vol. 56, no. 2, e2020RS007177. <https://doi.org/10.1029/2020RS007177>

[Link to publication on Research at Birmingham portal](#)

### **Publisher Rights Statement:**

An edited version of this paper was published by AGU. Copyright (2020) American Geophysical Union.

Forsythe, V. V., Azeem, I., Crowley, G., & Themens, D. R. (2021). Ionospheric vertical correlation distances: Estimation from ISR data, analysis, and implications for ionospheric data assimilation. *Radio Science*, 56, e2020RS007177. <https://doi.org/10.1029/2020RS007177>

### **General rights**

Unless a licence is specified above, all rights (including copyright and moral rights) in this document are retained by the authors and/or the copyright holders. The express permission of the copyright holder must be obtained for any use of this material other than for purposes permitted by law.

- Users may freely distribute the URL that is used to identify this publication.
- Users may download and/or print one copy of the publication from the University of Birmingham research portal for the purpose of private study or non-commercial research.
- User may use extracts from the document in line with the concept of 'fair dealing' under the Copyright, Designs and Patents Act 1988 (?)
- Users may not further distribute the material nor use it for the purposes of commercial gain.

Where a licence is displayed above, please note the terms and conditions of the licence govern your use of this document.

When citing, please reference the published version.

### **Take down policy**

While the University of Birmingham exercises care and attention in making items available there are rare occasions when an item has been uploaded in error or has been deemed to be commercially or otherwise sensitive.

If you believe that this is the case for this document, please contact [UBIRA@lists.bham.ac.uk](mailto:UBIRA@lists.bham.ac.uk) providing details and we will remove access to the work immediately and investigate.

# Radio Science

## RESEARCH ARTICLE

10.1029/2020RS007177

### Key Points:

- The ionospheric vertical correlation distances computed from IRI-2016 model errors are presented
- Vertical correlation distances increase exponentially with height and have an additional bump-on-tail enhancement
- New method for modeling the vertical component of covariance matrix that takes into account the asymmetry of correlations is proposed

### Correspondence to:

V. V. Forsythe,  
vforsythe@astraspace.net;  
victoriyaforforythe@gmail.com

### Citation:





Forsythe, V. V., Azeem, I., Crowley, G., & Themens, D. R. (2021). Ionospheric vertical correlation distances: Estimation from ISR data, analysis, and implications for ionospheric data assimilation. *Radio Science*, 55, e2020RS007177. <https://doi.org/10.1029/2020RS007177>

Received 31 JUL 2020

Accepted 20 OCT 2020

Accepted article online 23 OCT 2020

## Ionospheric Vertical Correlation Distances: Estimation From ISR Data, Analysis, and Implications For Ionospheric Data Assimilation

Victoriya V. Forsythe<sup>1</sup> , Irfan Azeem<sup>1</sup> , Geoff Crowley<sup>1</sup> , and David R. Themens<sup>2</sup> 

<sup>1</sup>ASTRA LLC., Louisville, CO, USA, <sup>2</sup>Department of Physics, University of New Brunswick, Fredericton, New Brunswick, Canada

**Abstract** The construction of the background covariance matrix is an important component of ionospheric data assimilation algorithms, such as Ionospheric Data Assimilation Four-Dimensional (IDA4D). It is a matrix that describes the correlations between all the grid points in the model domain and determines the transition from the data-driven to model-driven regions. The vertical component of this matrix also controls the shape of the assimilated electron density profile. To construct the background covariance matrix, the information about the spatial ionospheric correlations is required. This paper focuses on the vertical component of the model covariance matrix. Data from five different incoherent scatter radars (ISR) are analyzed to derive the vertical correlation lengths for the International Reference Ionosphere (IRI) 2016 model errors, because it is the background model for IDA4D. The vertical distribution of the correlations is found to be asymmetric about the reference altitude around which the correlations are calculated, with significant differences between the correlation lengths above and below the reference altitude. It is found that the correlation distances not only increase exponentially with height but also have an additional bump-on-tail feature. The location and the magnitude of this bump are different for different radars. Solar flux binning introduces more pronounced changes in the correlation distances in comparison to magnetic local time (MLT) and seasonal binning of the data. The latitudinal distribution of vertical correlation lengths is presented and can be applied to the construction of the vertical component of the background model covariance matrix in data assimilation models that use IRI or similar empirical models as the background.

### 1. Introduction

The background error covariance matrix  $\tilde{P}_f$  is an important component of ionospheric data assimilation. It describes the variance of the background model used for the assimilation and how the errors of this model correlate between any two grid points. Each element of the model error covariance matrix  $\tilde{P}$  can be expressed the following way:

$$\tilde{P}_{ij} = \sigma_i \sigma_j r_{ij}, \quad (1)$$

where  $\sigma_i$  and  $\sigma_j$  are the standard deviations of the forecast model values at  $i$ th and  $j$ th grid points and  $r_{ij}$  is the linear correlation coefficient between these errors.

In practice, it is close to impossible to find the real representation of this matrix for several reasons. First, the true values of the electron density at all grid points on the globe are unknown. Second, the error covariance matrix  $\tilde{P}$  is usually a very large matrix of size  $n \times n$ , where  $n$  is the number of grid points in the assimilation. Even if, hypothetically, the truth would be known, it can be too computationally demanding to calculate  $\tilde{P}$  for each time step of the assimilation. Therefore, in practice, this error covariance matrix needs to be modeled a priori. Typically, three assumptions are used for modeling the error covariance matrix (Aa et al., 2015, 2016; Bust & Crowley, 2007; Bust & Datta-Barua, 2014; Bust et al., 2001, 2004; Coker et al., 2001; Yue, Wan, Liu, Zheng, et al., 2007; Yue et al., 2011). First, the spatial correlation is assumed to be separable horizontally and vertically. Second, the vertical correlations are represented by a Gaussian. Third, the horizontal correlations are modeled by an elliptical Gaussian in geomagnetic coordinates.

Using these three assumptions, the construction of the error covariance matrix  $\tilde{P}$  can be separated into the construction of three matrices: the model variance matrix  $\tilde{V}$ , the horizontal correlation matrix  $\tilde{C}_{hor}$ , and the

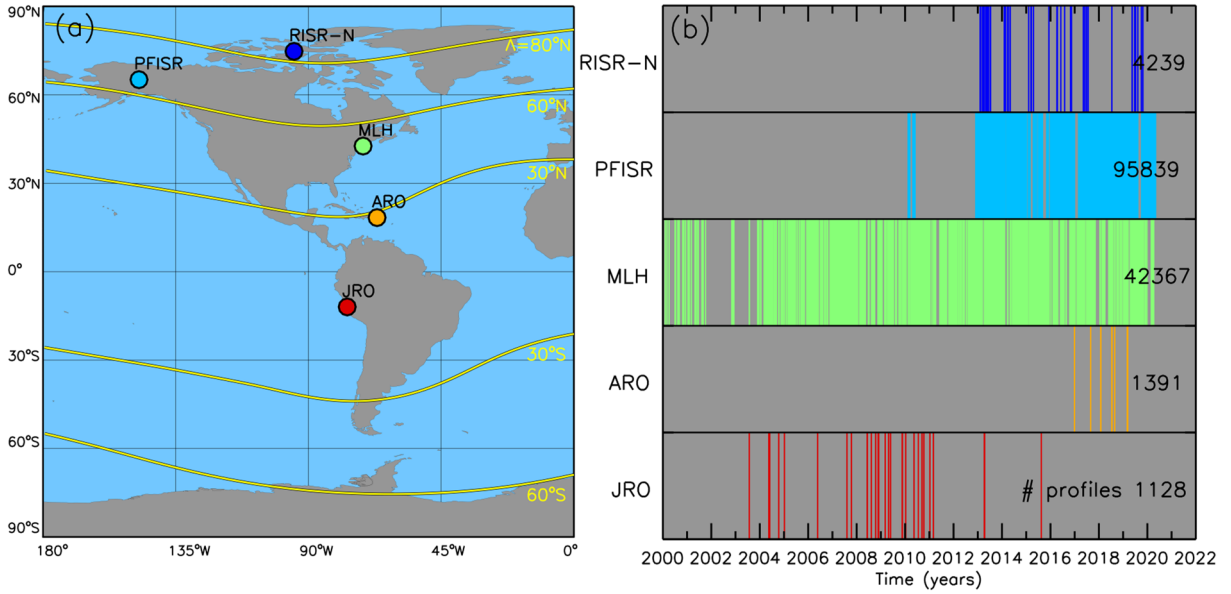


**Figure 1.** Experimental setup and data coverage. (a) Locations of ISRs are shown with circles. Yellow lines show 80°N, 60°N, 30°N, 30°S, and 60°S geomagnetic latitudes. (b) Data coverage of ISR data. The number of profiles after filtering are shown on the right of the panel.

vertical correlation matrix  $\tilde{C}_{ver}$ . The elements  $\tilde{P}_{ij}$  can then be found using element by element multiplication:

$$\tilde{P} = \tilde{V} \circ \tilde{C}_{hor} \circ \tilde{C}_{ver}. \quad (2)$$

Forsythe et al. (2020) discussed in detail the construction of the horizontal correlation matrix  $\tilde{C}_{hor}$ . The construction of the vertical correlation matrix  $\tilde{C}_{ver}$  is treated in this paper.

Bust et al. (2001) first suggested to model the vertical correlation matrix as a Gaussian

$$\tilde{C}_{ij}^{ver} = \exp \left[ -\frac{(z_i - z_j)^2}{L_z^i L_z^j} \right], \quad (3)$$

where  $z$  is the height and  $L_z$  is the vertical correlation length for grid points  $i$  and  $j$ .

Previously, the vertical correlation length  $L_z$  was approximated by the ionospheric scale height (Bust et al., 2004) and has not been derived for any particular background model. In practice, and as will be shown in this paper, the height variation of vertical correlation distances derived from model errors can be more complicated than the ionospheric scale height variation.

In this study, the parameters that describe the latitudinal distribution of the vertical ionospheric correlations are derived for the first time. Importantly, this is the first study that is dedicated to the vertical correlation of the International Reference Ionosphere 2016 (IRI) (Bilitza et al., 2017) model errors using multiple instruments located at different latitudinal regions. The results of this study can be directly applied to the construction of the error covariance matrix for various data assimilation models (Forsythe, 2020) that use IRI or other similar empirical models as the background.

## 2. Experimental Setup

The data from five incoherent scatter radars (ISR) were analyzed in this study to calculate the vertical correlation lengths. Figure 1a shows the locations of Jicamarca (JRO), Arecibo (ARO), Millstone Hill (MLH), Poker Flat ISR (PFISR), and Resolute Bay North ISR (RISR-N). The yellow lines show the 80°N, 60°N, 30°N, 30°S, and 60°S geomagnetic latitudes, based on the altitude-adjusted corrected geomagnetic (AACGM) coordinate system with 2010 coefficients (Shepherd, 2014). In this study we use all available data where the radars observed the vertical distribution of the electron density for the time period starting from the year of 2000. The following ISR modes were chosen: Long Pulse (LP) Mode for RISR-N and PFISR, Oblique Mode Faraday Rotation With Uncoded LP (Hybrid 2) for JRO, and Coded LP Mode mode for ARO. For the MLH

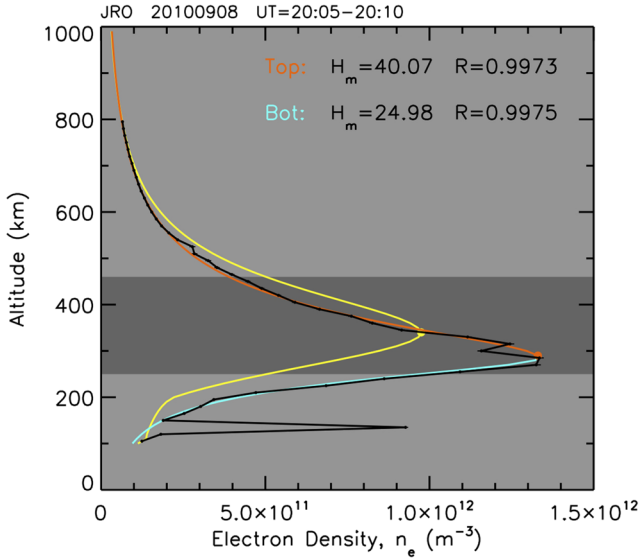


**Figure 2.** Observed EDP from the JRO radar on 8 September 2010 at 20:05–20:10 UT shown in black solid lines. The error bars are also shown but are usually significantly smaller than the circles representing the data points. The IRI profile for this time period is shown in yellow. The dark gray area shows the altitudinal range where IRI profile is greater than half of IRI  $N_m F_2$  (shown with the yellow circle). The  $N_m F_2$  of the observed profile is found as the maximum density within the gray area and is shown with orange circle. Orange and cyan lines show the top fit and bottom fit with scale heights  $H_m$  and correlation coefficients to the data points  $R$  also shown in the panel.

profile. The IRI EDP for the location of the radar and for the same time period as the measurement is shown as the yellow curve in Figure 2. The altitudinal range where the IRI density is greater than half of  $N_m F_2$  (shown with the yellow circle) was determined and highlighted in the figure with dark gray color background. The peak of the observed profile was found within this altitudinal range and is shown with an orange circle. In case the calculated peak of the profile was located at the upper (lower) boundary of the gray area, the altitudinal range was shifted up (down) by 100 km (50 km) up (down) and the location of the density maximum was found again. This method was applied to avoid cases where the density maximum is located in the  $E$  region due to sporadic  $E$  events and particle precipitation. Once the  $N_m F_2$  value was determined, the Chapman model described by Equation 4

$$N_e(h) = N_m F_2 \exp \left[ 0.5 \left( 1 - \frac{h - h_m F_2}{H(h)} - \exp \left( -\frac{h - h_m F_2}{H(h)} \right) \right) \right] \quad (4)$$

was fitted to the data using the least squares method by Markwardt (2009). For the topside ionosphere, the scale height is given by:

$$H(h) = A_1(h - h_m F_2) + H_{m1}. \quad (5)$$

This approach to modeling the topside has been applied before, demonstrating acceptable performance below 1,200-km altitudes (dos Santos Prol et al., 2019). For the bottomside ionosphere, the expression for the scale height is as follows:

$$H(h) = A_2(h - h_m F_2) + H_{m2}. \quad (6)$$

Here,  $h$  is the height and  $A_1$ ,  $A_2$ ,  $H_{m1}$ , and  $H_{m2}$  are the fitting coefficients. Additionally, we also constrained the  $A_1$  parameter to positive values only. The orange and cyan lines in Figure 2 show the fitted profile for the topside and bottomside, respectively. Since this study focuses only on the  $F$  region portion of the profile, the omission of the  $E$  region layer in the model is deliberate and does not impact our results. The following criteria were used to filter out poor quality profiles: The number of data points for the topside is below 5

ISR, we use the data provided in the “gridded data filtered to a uniform spatial and temporal grid” format, which are derived from raw zenith measurements.

For all radars listed above, only the vertical profiles were selected for the analysis presented here. For PFISR the vertically oriented beam was tagged as 64280. For RISR-N the beam with elevation angle of  $75^\circ$  and azimuth of  $26^\circ$  was selected over the beam with  $90^\circ$  elevation because the vertical beam has a grating lobe issue. The data from MLH and ARO used in this study were collected at elevation angles of  $89.74^\circ$  and  $90^\circ$ , respectively. The lowest elevation angle for the JRO radar data was  $87.06^\circ$ . Figure 1b shows the data coverage for all radars. PFISR had the highest number of observations, and MLH had the most continuous coverage between 2000 and 2020. In this study, the binning of data in magnetic local time (MLT), season, and  $F10.7$  will be only applied to MLH radar because of the continuity of the data set. All radars had different maximum ranges. The maximum ranges for JRO, ARO, MLH, PFISR, and RISR-N are 1,635, 687, 547.85, 673.3, and 692.34 km, respectively.

### 3. Data Preprocessing

The first step of the analysis included the uniform gridding of the ISR data into 5-min intervals, excluding MLH that was already gridded into 15-min intervals. Next, the two-layer Chapman function (Rishbeth & Garriott, 1969) was fitted to each of the individual profiles. Figure 2 shows one example of the fitted Chapman model to the JRO measurements on 8 September 2010 at 20:05–20:10 UT. The measured electron density profile (EDP) with uncertainties is shown in black. In this particular time frame the uncertainties are very small and are visible only near the peak of the

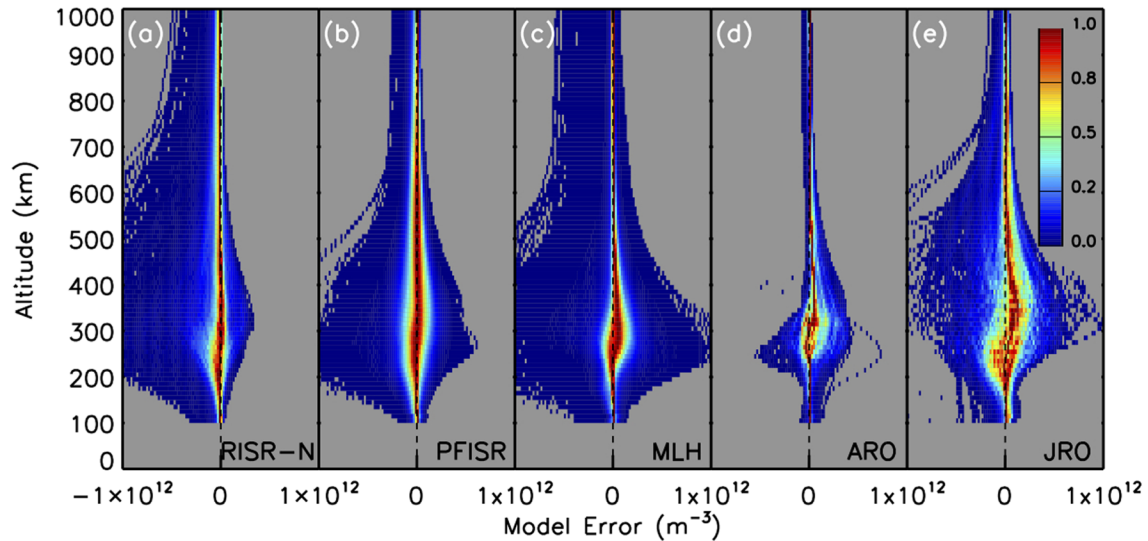


**Figure 3.** (a–e) Distributions of IRI model errors normalized by the total amount of EDP profiles for each radar.

and for the bottomside is below 3, the  $H_{m1}$  or the  $H_{m2}$  is less than 0 or greater than 150, and the correlation coefficient between the data points and corresponding fitted points is less than 0.8. Additionally, several profiles that had negative scale height in the bottomside were excluded. Figure 1b showed the number of profiles that remained after the filtering procedure. Uncertainties for the data points were considered in the fitting procedure using normal weighting. In case the data point did not have any information about the error, it was set to 20% of the observed value.

Finally, the differences between the IRI profiles (obtained with default IRI model options) and the fitted profiles were calculated and are referred to as model errors hereafter. Figure 3 shows the distribution of model errors for all radars, normalized by the maximum number of EDPs for each radar. The peaks of the distributions of model errors for most altitudes are centered around zero. There exist some shifts of the distributions for the altitude range between 200 and 400 km. For example, the MLH radar  $F$  region densities are lower in comparison to IRI, as shown in Figure 3c. The data-model differences are largest at JRO, which show negative model errors below 300-km altitude and positive errors above (Figure 3e). The tails of the distributions are very long, exceeding  $1 \times 10^{12} \text{ m}^{-3}$  for RISR-N, PFISR, MLH, and JRO radars, indicating that a small fraction of EDPs strongly disagreed with the model. Interestingly, the RISR-N tails of the distributions are predominantly negative, as can be seen in Figure 3a. This is consistent with the previous studies (Bjoland et al., 2016; Themens et al., 2014) that concluded that the IRI model is biased toward an underestimation of the electron density in the polar cap.

#### 4. Results

The correlations between the model errors at different heights were calculated using preprocessed data for all radars, without any binning of the data. Here we describe our analysis in more detail. For each ISR shown in Figure 3, the linear correlation coefficients are found between the model errors at a reference height with those at other heights. These correlations are calculated for a range of reference altitudes between 100 and 1,000 km. Figures 4a–4e show the calculated correlations for all radars, with the color bar shown in panel (a). The  $x$  axis is the reference altitude, and the  $y$  axis corresponds to the distance (positive is along the upward direction) from the reference point. The dashed white line at 200-km altitude indicates the beginning of the altitudinal range where the fitted Chapman function agrees well with the data points. Even if the data were available below this altitude, the  $E$  region layer was not reflected in the fitted profile. The second white dashed line indicates the maximum altitude where the radar data were available. It is different for each radar. The maximum altitude of the JRO radar data is 1,635 km; this is why the second line is not shown. The solid (dashed) black line shows the contour of 0.7 correlation using only the points above (below) the reference point. This distance, where the correlation is equal to 0.7, is defined as the correlation length for the purpose of this study. In this paper we will keep using the same formalism and will define the correlation length as

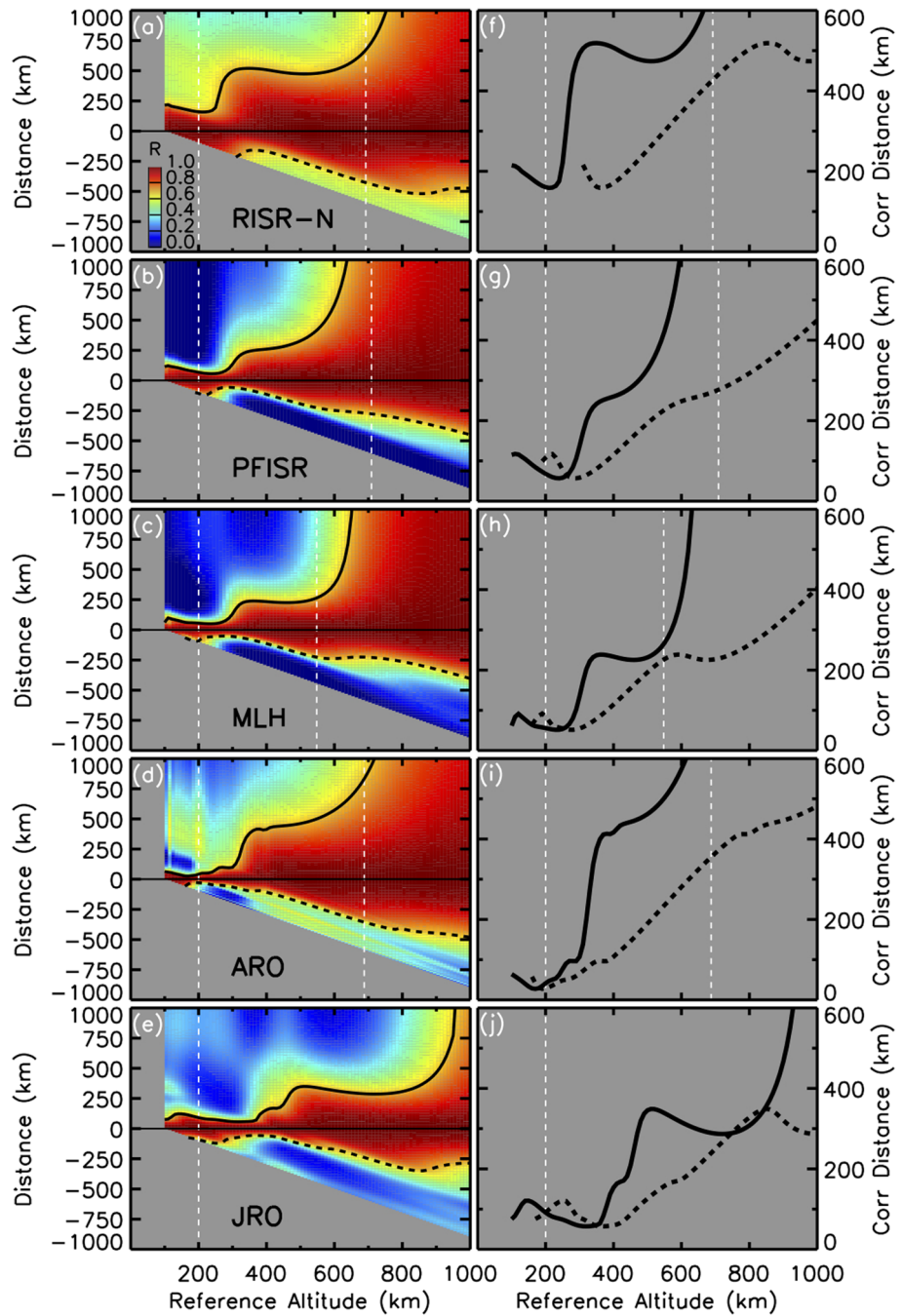


**Figure 4.** Vertical correlations of IRI model errors and derived correlation length. (a–e) The color shows the correlations of IRI errors between reference altitude and all other points of the EDP, with the color bar shown in panel (a). Solid (dashed) black line shows the contour of 0.7 correlation for the points above (below) the reference point. Each row corresponds to the different radar, with the name of the radar shown at each panel. (f–j) Vertical correlation distances above and below the reference altitude are shown with solid and dashed black lines, respectively. White dashed lines in all panels indicate the regions driven by the radar data.

a distance where the linear correlation coefficient is equal to 0.7. Figures 4f–4j show the estimated vertical correlation length based on our formalism for each radar site. Again, the solid (dashed) line corresponds to the correlation length for the points above (below) the reference point.

From Figure 4 it is evident that the correlation lengths derived for upward and downward direction are very different and that this asymmetry needs to be taken into account for the modeling of the vertical covariance

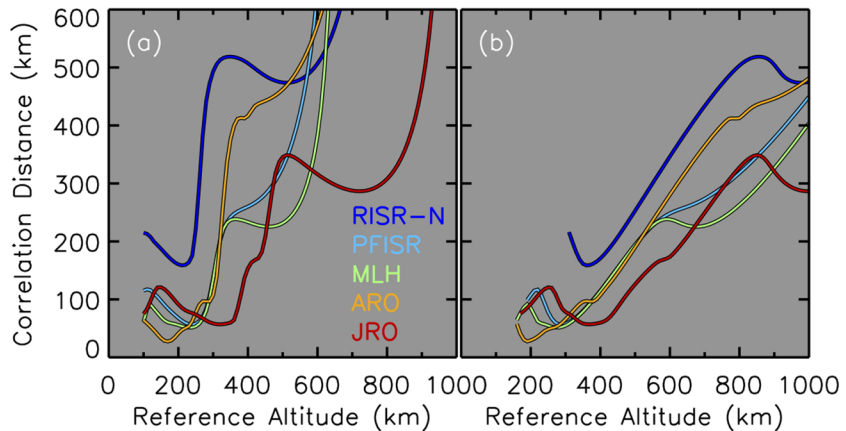
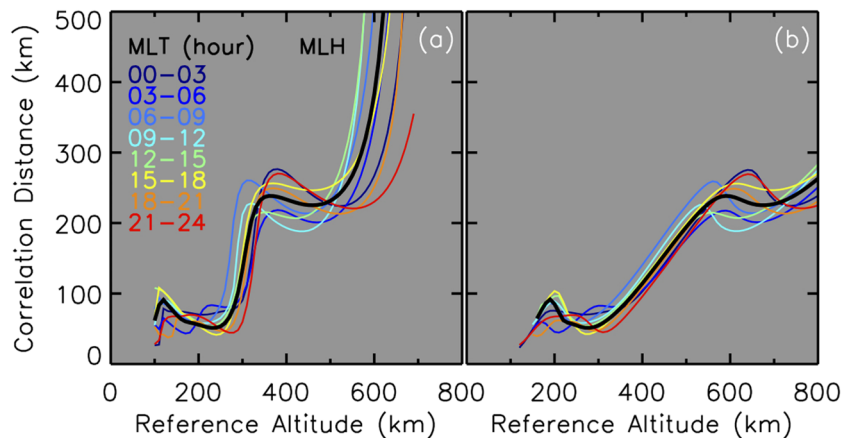


**Figure 5.** Vertical correlation distances derived from IRI model errors (a) above and (b) below the reference altitude for all radars, indicated by the color.

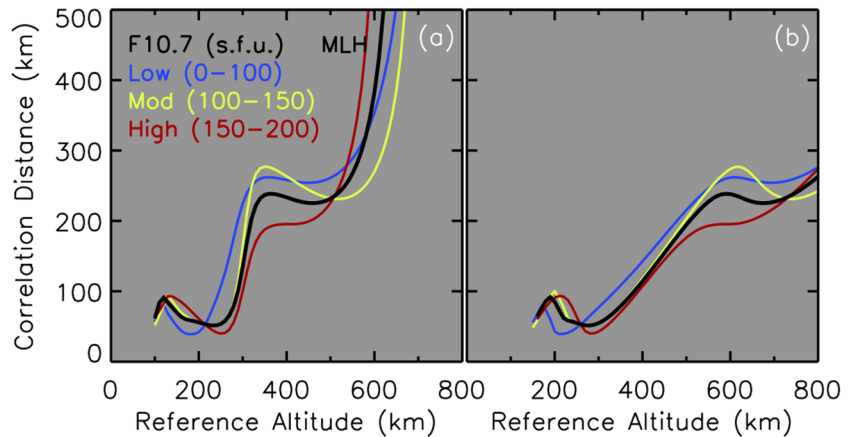
matrix. The correlation length derived from model errors exhibits a complex structure, with a well-defined bump-on-tail like shape, where the bump is centered at different reference altitudes for different radars.

Figure 5 compares the calculated vertical correlation lengths from different radars. The colors of the lines correspond to different radars. All correlation distances, except those computed from the JRO radar data, exhibit exponential increases starting around 200-km altitude. For the JRO radar site, the vertical correlation distances show exponential growths starting near 350 km for positive distances and 400 km for negative distances from the reference altitude, as shown in Figure 5. RISR-N correlation distances also start the exponential increase from 400 km for negative distances. In general, the sharpness of the exponential increase, the height of the bump, and location with respect to the reference altitude are different for each radar. Only PFISR and MLH correlation distances exhibit similar behavior.

Next, the variations of the vertical correlation distances for different diurnal, seasonal, and solar conditions are evaluated. Only the MLH data were used for this evaluation, because it was the only site that provided continuity of data coverage needed to examine the seasonal and solar flux influence on the correlation lengths. To evaluate the diurnal variation of the vertical correlation distances, the MLH data were divided into 3-hour MLT bins. In Figure 6 the colors of the lines represent different MLT bins, and the thick black line shows the correlation distance without binning. The trends look the same for all MLT bins, with minor differences in the position of the bump and the slope of the exponential increase. Both positive and negative distances from the reference altitude, shown in Figure 6, show similar behaviors with MLT.



**Figure 6.** Vertical correlation distances derived from IRI model errors (a) above and (b) below the reference altitude for MLH radar data binned in MLT, indicated by the color. Thick black line shows correlation distances for un-binned in MLT data.



**Figure 7.** Vertical correlation distances derived from IRI model errors (a) above and (b) below the reference altitude for MLH radar data binned in  $F10.7$ , indicated by the color. Thick black line shows correlation distances for data not divided into  $F10.7$  bins.

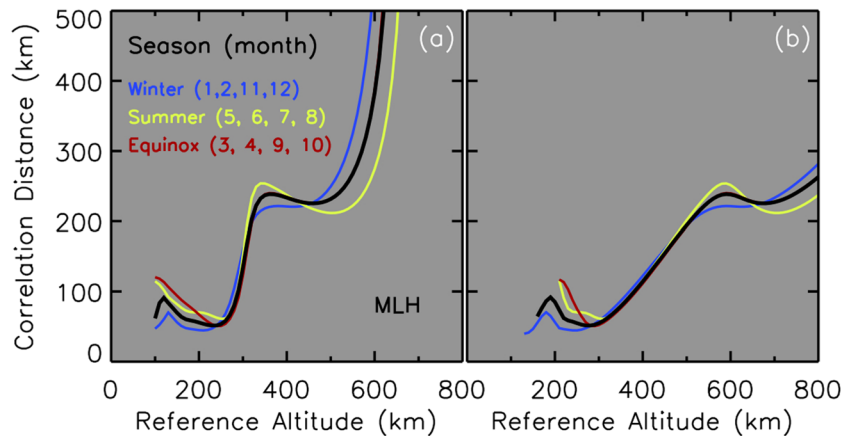
Figure 7 shows the vertical correlation distances computed using the MLH radar data for low, moderate, and high values of  $F10.7$  solar flux index, represented by different colors. The solar flux influence is more pronounced than the MLT variation. For the correlation distances above the reference point (Figure 7a) the high solar flux reduces the height of the bump and increases the exponential slope, whereas during low and moderate  $F10.7$  values the bumps have a similar shape and height. The reference altitude position of the bump does not change across the different solar flux bins. For the correlation distances below the reference point (Figure 7b) the position of the bump shows similar change with solar flux, but in addition, the reference altitude of the bump is shifting as well.

Additionally, the seasonal dependence of vertical correlation distances is investigated. Figure 8 shows the vertical correlation distances for MLH radar for winter, summer, and equinox seasons. The variations with different seasons are very minor, as demonstrated in Figure 8.

### 5. Application to Data Assimilation

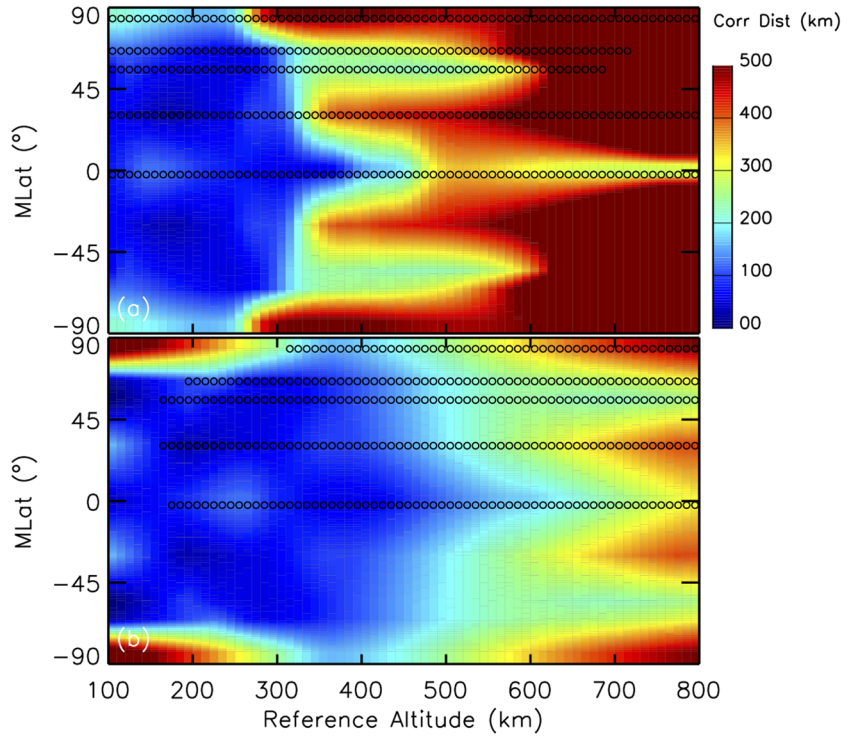
To model the vertical correlation distance for data assimilation purposes, only the unbinned data, shown in Figure 5, were considered. When more data are available for the equatorial and polar cap regions, the binning in MLT, season, and solar flux can be incorporated into the modeling.

Figure 9 shows the modeled distribution of the vertical correlation distances as a function of magnetic latitude. Figure 9a and b corresponds to the correlation distances above (below) the reference point. The color in



**Figure 8.** Vertical correlation distances derived from IRI model errors (a) above and (b) below the reference altitude for MLH radar data binned in season, indicated by the color. Thick black line shows correlation distances for unbinned in season data.





**Figure 9.** Latitudinal distribution of modeled vertical correlation length (a) above and (b) below the reference altitude. The color indicates the correlation distance, with the color bar shown on the right. The circles show the data-derived points for the locations of the ISRs, same information as in Figure 5. These results can be download at data repository (Forsythe, 2020).

Figure 9 indicates the correlation distance, with the color bar shown on the right. The correlation distances are modeled using linear interpolation between the data-derived points, shown with circles in Figure 9. These data-derived points are the same as in Figure 5, and their magnetic latitude locations correspond to the locations of the ISRs. Northern Hemisphere values are reflected into the Southern Hemisphere in the absence of Southern Hemisphere radar data.

Then each element of the vertical correlation matrix for the construction of the background covariance matrix can be modeled as

$$\tilde{C}_{ij}^{ver} = \begin{cases} \exp \left[ -\frac{(z_i - z_j)^2}{(L_1(z_i, \lambda_i))^2} \right], & \text{if } z_i < z_j \\ \exp \left[ -\frac{(z_i - z_j)^2}{(L_2(z_i, \lambda_i))^2} \right], & \text{if } z_i > z_j, \\ 1, & \text{if } z_i = z_j \end{cases} \quad (7)$$

where  $z$  is the height,  $\lambda$  is the magnetic latitude,  $L_1$  and  $L_2$  are functions of altitude and magnetic latitude, and subscripts  $i$  and  $j$  refer to the pairs of grid points.  $L_1$  and  $L_2$  are presented in Figures 9a and 9b and are provided in the form of metadata.

## 6. Discussion

### 6.1. The Position of the Bump

Based on previous studies, a simple exponential increase of the correlation distances with height was anticipated. For example, Yue, Wan, Liu, and Mao (2007) analyzed vertical correlations derived from day-to-day ionospheric variability using MLH data and reported an exponential increase of correlation distance with height, even though they used a fitting scheme similar to the one in this study. The increase of the ionospheric scale height was also assumed to be exponential (Bust et al., 2004; Yue et al., 2011) without a bump-on-tail local maximum. This study shows that the correlation distances exhibit a more complex

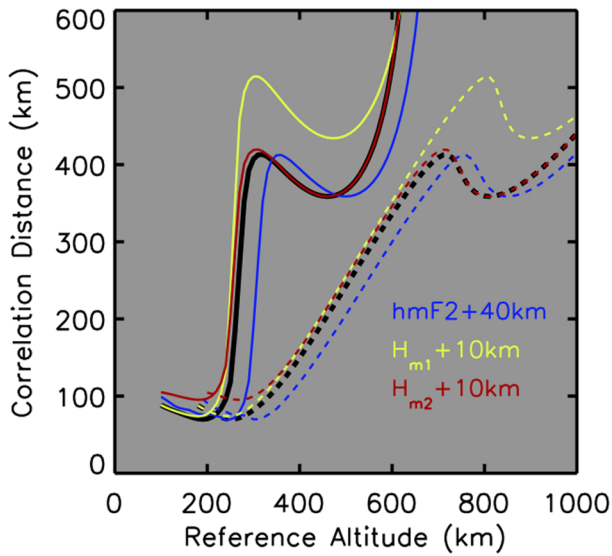


**Figure 10.** Correlation distances calculated from MLH data without any removal of the corresponding IRI modeled values or day-to-day variability. Solid (dashed) lines correspond to the upward (downward) direction from the reference point. Black lines show the correlation distances derived from unmodified MLH data, whereas blue, yellow, and red lines correspond to the following modifications:  $hmF2+40$  km,  $H_{m1}+10$  km, and  $H_{m2}+10$  km, respectively.

behavior. Two new features were observed. First, the presence of asymmetry around the reference point was found. Second, the presence of a bump-on-tail correlation distance structure was reported.

To better understand the behavior of the vertical correlation distances, a few simplified scenarios were considered. Using the vertical EDPs from MLH, the vertical upward and downward correlation distances were first calculated without any removal of the corresponding IRI modeled values or day-to-day variability, shown in Figure 10 with black solid and dashed lines. Even in this scenario where diurnal and seasonal time scales dominate, we still see the characteristic bump-on-tail correlation distance structure. This suggests that this structure has more to do with the general vertical structure of the ionosphere than the type of variability experienced.

To understand what parameter controls the position of the bump, the  $hmF2$  of the MLH profiles was increased by 40 km and separately  $H_{m1}$  and  $H_{m2}$  were increased by 10 km. The correlation distances from these systematically perturbed MLH profiles are presented in Figure 10 with blue, yellow, and red lines, respectively. The location of the bump and the correlation distance curve, as a whole, is directly influenced by  $hmF2$ . Similarly, the  $H_m$  terms directly influence the magnitude of the correlation distances in their region of influence (separately above and below  $hmF2$ ).

## 6.2. Comparison With Vertical Correlation Length Derived From Day-to-Day Ionospheric Variability

In the previous investigation of the horizontal correlation distances (Forsythe et al., 2020), a significant difference was found between the correlation distances derived from the IRI errors and from day-to-day total electron content (TEC) variability. It was concluded that the day-to-day variability-derived correlation length cannot be employed for the modeling of the background error covariance matrix. Similarly here, to investigate the differences between the vertical correlation lengths derived using these two approaches, the following analysis is performed. The day-to-day variability of electron density (the difference between two consecutive days) was calculated using fitted EDPs for MLH, and the correlation distances were found using the same method described in section 3. Figure 11 shows the results of the comparison. The blue (red) color corresponds to the correlation distances derived from IRI model errors (day-to-day electron density variability). The differences between the two results are very minor. This suggests that the day-to-day ionospheric variability is one of the important factors that controls the vertical distribution of model error correlations.

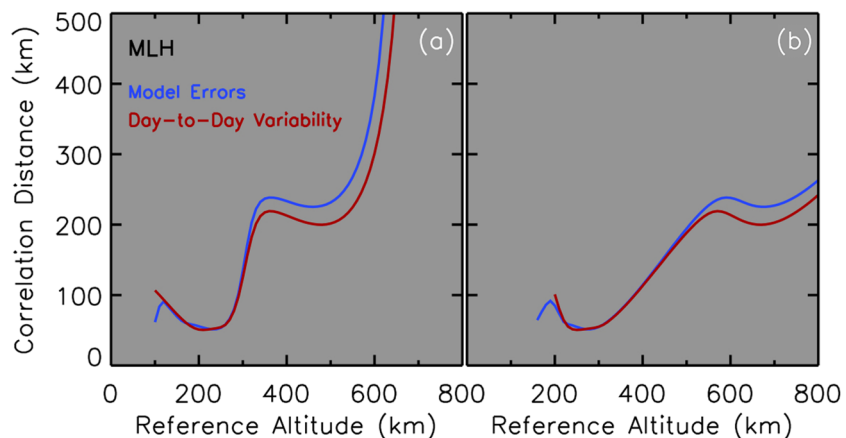


**Figure 11.** Comparison of vertical correlation length (a) above and (b) below the reference altitude derived from IRI model errors and electron density day-to-day variability for MLH data. The color indicates the method of derivation.

## 7. Conclusions

The IRI-2016 model errors were calculated using data from five ISRs, and the vertical correlation distances were computed from the distributions of model errors. It was found that the vertical distribution of the correlations is asymmetric and that it is important to estimate the vertical correlation distance in two directions, above and below the reference point. The correlation distances increase exponentially with height and have an additional bump-on-tail enhancement. The reference altitude and height of this bump are different for all radars. The position of the bump is controlled by the  $hmF2$  and  $H_m$  parameters. The changes with MLT and season for MLH radar are not significant, but the solar flux binning introduces more pronounced changes (about 100-km difference in the height of the bump for high and low solar flux). The latitudinal distribution of vertical correlation length was modeled and is available at Forsythe (2020). This distribution can be applied to the construction of vertical component of the background model covariance matrix. In a future study, the horizontal and vertical correlation lengths will be implemented in the Ionospheric Data Assimilation Four-Dimensional (IDA4D) algorithm to examine their effects on the assimilation results.

## Data Availability Statement

All ISR data were obtained through Madrigal Database (<http://isr.sri.com/madrigal/>). The vertical correlation lengths for different latitudes and heights derived in this study are available online (<https://doi.org/10.5281/zenodo.3928823>).

## Acknowledgments

The Arecibo Observatory is the principal facility of the National Astronomy and Ionosphere Center, which is operated by the Cornell University under a cooperative agreement with the National Science Foundation. The Jicamarca Radio Observatory is a facility of the Instituto Geofísico del Perú and is operated with support from the National Science Foundation Cooperative Agreements through Cornell University. The Millstone Hill incoherent scatter radar is supported by the National Science Foundation. PFISR and RISR-N are operated by SRI International under NSF Cooperative Agreement.

## References

- Aa, E., Huang, W., Yu, S., Liu, S., Shi, L., Gong, J., et al. (2015). A regional ionospheric TEC mapping technique over China and adjacent areas on the basis of data assimilation. *Journal of Geophysical Research: Space Physics*, *120*, 5049–5061. <https://doi.org/10.1002/2015JA021140>
- Aa, E., Liu, S., Huang, W., Shi, L., Gong, J., Chen, Y., et al. (2016). Regional 3-D ionospheric electron density specification on the basis of data assimilation of ground-based GNSS and radio occultation data. *Space Weather*, *14*, 433–448. <https://doi.org/10.1002/2016SW001363>
- Bilitza, D., Altadill, D., Truhlik, V., Shubin, V., Galkin, I., Reinisch, B., & Huang, X. (2017). International reference ionosphere 2016: From ionospheric climate to real-time weather predictions. *Space Weather*, *15*, 418–429. <https://doi.org/10.1002/2016SW001593>
- Bjoland, L. M., Belyey, V., Lovhaug, U. P., & La Hoz, C. (2016). An evaluation of international reference ionosphere electron density in the polar cap and cusp using EISCAT Svalbard radar measurements. *Annales Geophysicae*, *34*, 751–758. <https://doi.org/10.5194/angeo-34-751-2016>
- Bust, G. S., Coco, D. S., & Gaussiran, T. L. II (2001). Computerized ionospheric tomography analysis of the combined ionospheric campaign. *Radio Science*, *36*(6), 1599–1605. <https://doi.org/10.1029/1999RS002424>
- Bust, G. S., & Crowley, G. (2007). Tracking of polar cap ionospheric patches using data assimilation. *Journal of Geophysical Research*, *112*, A05307. <https://doi.org/10.1029/2005JA011597>
- Bust, G. S., & Datta-Barua, S. (2014). Scientific investigations using IDA4D and EMPIRE. In *Modeling the ionosphere-thermosphere system* (1st ed., chap. 23, pp. 283–297). Chichester, UK: John Wiley & Sons, Ltd. <https://doi.org/10.1002/9781118704417>
- Bust, G. S., Garner, T. W., & Gaussiran, T. L. (2004). Ionospheric data assimilation three-dimensional (IDA3D): A global, multisensor, electron density specification algorithm. *Journal of Geophysical Research*, *109*, A11312. <https://doi.org/10.1029/2003JA010234>
- Coker, C., Kronschnabl, G., Coco, D. S., Bust, G. S., & Gaussiran, T. L. II (2001). Verification of ionospheric sensors. *Radio Science*, *36*(6), 1523–1529. <https://doi.org/10.1029/1999RS002418>
- dos Santos Prol, F., Themens, D. R., Hernandez-Pajares, M., de Oliveira Camargo, P., & Tadeu de Assis Honorato Muella, M. (2019). Linear vary-chap topside electron density model with topside sounder and radio-occultation data. *Surveys in Geophysics*, *40*, 277–293. <https://doi.org/10.1007/s10712-019-09521-3>
- Forsythe, V. (2020). Ionospheric vertical correlation length derived from IRI-2016 model errors. <https://doi.org/10.5281/zenodo.3928823>
- Forsythe, V. V., Azeem, I., & Crowley, G. (2020). Model covariance matrix formation: Horizontal correlation length. CEDAR 2020, Virtual Meeting <https://drive.google.com/file/d/1OXkE3fQbV3uSKo4VGsgRNdfXB9aYBMel/view>
- Markwardt, C. B. (2009). Astronomical data analysis software and systems XVIII. 411,251.
- Rishbeth, H., & Garriott, O. K. (1969). *Introduction to ionospheric physics*. San Diego, CA: Academic Press.
- Shepherd, S. G. (2014). Altitude-adjusted corrected geomagnetic coordinates: Definition and functional approximations. *Journal of Geophysical Research: Space Physics*, *119*, 7501–7521. <https://doi.org/10.1002/2014JA020264>
- Themens, D. R., Jayachandran, P. T., Nicolls, M. J., & MacDougall, J. W. (2014). A top to bottom evaluation of IRI 2007 within the polar cap. *Journal of Geophysical Research: Space Physics*, *119*, 6689–6703. <https://doi.org/10.1002/2014JA020052>
- Yue, X., Schreiner, W. S., Lin, Y.-C., Rocken, C., Kuo, Y.-H., & Zhao, B. (2011). Data assimilation retrieval of electron density profiles from radio occultation measurements. *Journal of Geophysical Research*, *116*, A03317. <https://doi.org/10.1029/2010JA015980>
- Yue, X., Wan, W., Liu, L., & Mao, T. (2007). Statistical analysis on spatial correlation of ionospheric day-to-day variability by using GPS and incoherent scatter radar observations. *Annales Geophysicae*, *25*, 1815–1825.
- Yue, X., Wan, W., Liu, L., Zheng, F., Lei, J., Zhao, B., et al. (2007). Data assimilation of incoherent scatter radar observation into a one-dimensional midlatitude ionospheric model by applying ensemble Kalman filter. *Radio Science*, *42*, RS6006. <https://doi.org/10.1029/2007RS003631>